

RESEARCH ARTICLE | MAY 10 2024

Mitigating inflow acceleration effects in twin mountains using air jets: Emphasis on anti-wind for high-speed railways



Special Collection: [Flow and Civil Structures](#)

Jian Wang (王剑) ; E Deng (邓铿) ; Yi-Qing Ni (倪一清); Xu-Hui He (何旭辉) ; Pak-Wai Chan (陈柏纬); Wei-Chao Yang (杨伟超); Huan Li (李欢) ; Zu-Yu Xie (谢祖育)



Physics of Fluids 36, 055128 (2024)

<https://doi.org/10.1063/5.0202419>



Articles You May Be Interested In

Acceleration and Reynolds effects of crosswind flow fields in gorge terrains

Physics of Fluids (August 2023)

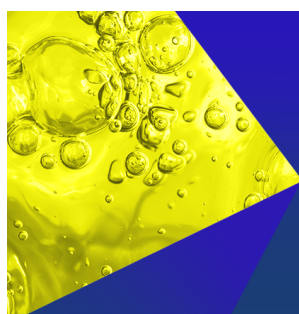
Flow dynamics of train under turbulent inflow at different crosswind yaw angles

Physics of Fluids (March 2024)

Effects of windbreak types on aerodynamics of high-speed trains traversing from flat ground to semi-cutting and semi-embankment under crosswinds

Physics of Fluids (July 2024)

21 May 2025 08:22:27



Physics of Fluids
Special Topics
Open for Submissions

[Learn More](#)

Mitigating inflow acceleration effects in twin mountains using air jets: Emphasis on anti-wind for high-speed railways

Cite as: Phys. Fluids **36**, 055128 (2024); doi: [10.1063/5.0202419](https://doi.org/10.1063/5.0202419)

Submitted: 4 February 2024 · Accepted: 9 April 2024 ·

Published Online: 10 May 2024





View Online



Export Citation



CrossMark

Jian Wang (王剑),^{1,2}  E Deng (邓铿),^{2,3,4,a)}  Yi-Qing Ni (倪一清),^{3,4} Xu-Hui He (何旭辉),^{1,5}  Pak-Wai Chan (陈柏纬),⁶ Wei-Chao Yang (杨伟超),^{1,5} Huan Li (李欢),^{1,5}  and Zu-Yu Xie (谢祖育)¹

AFFILIATIONS

¹School of Civil Engineering, Central South University, Changsha, People's Republic of China

²The Hong Kong Polytechnic University Shenzhen Research Institute, Shenzhen, People's Republic of China

³National Rail Transit Electrification and Automation Engineering Technology Research Center (Hong Kong Branch), Hong Kong, People's Republic of China

⁴Department of Civil and Environmental Engineering, The Hong Kong Polytechnic University, Hong Kong, People's Republic of China

⁵National Engineering Research Center of High-speed Railway Construction Technology, Changsha, People's Republic of China

⁶Hong Kong Observatory, Hong Kong, China

Note: This paper is part of the special topic, Flow and Civil Structures.

^{a)} Author to whom correspondence should be addressed: early.deng@polyu.edu.hk

ABSTRACT

The twin mountains, a common terrain in mountainous areas, tend to induce the acceleration effect under crosswinds, which enhances the wind speed and the turbulence performance of the flow field. To mitigate the impact of the acceleration effect on high-speed trains, structures, and aircraft near the twin mountains, this study investigates the effectiveness of the jet strategies, which are realized on natural mountain slopes by mechanical ventilation, with different jet angles on the flow field and the train. Wind speed tests, flow visualization, wind field prediction, and research on the train's aerodynamic behavior are conducted in this paper using the wind tunnel and the improved delayed detached eddy simulation dynamic models. The results indicate that the wind velocity on the leeward side of the twin mountains increases up to 1.42 folds of the wind velocity of the incoming flow under crosswinds. The jet streams with 0° and 30° angles are the most effective in mitigating the acceleration effect among those tested (0°, 15°, 30°, and 45°), reducing the maximum wind speed by 11.87% and 16%, respectively. Compared with the mitigation effect of the jet stream with the 30° angle, the jet stream with the 0° angle has a better mitigation effect on the aerodynamic loads (4.0%–13.2%) and its fluctuation amplitude (24.4%–42.7%) of the train. These findings are valuable for studying the flow field characteristics of the twin mountains and the designing anti-wind measures for high-speed railways.

Published under an exclusive license by AIP Publishing. <https://doi.org/10.1063/5.0202419>

I. INTRODUCTION

In the atmosphere, the acceleration effect occurs when flows pass through narrow geographical features or buildings.^{1,2} As the flows pass through these narrow areas, the velocity of the flows increases significantly. Specifically, as shown in Fig. 1(a), the twin mountainous terrain prevalent in mountainous regions produces a significant acceleration effect under crosswinds. The characteristics of the flow field of the twin mountains are unevenly distributed in spatial and temporal scales.^{3,4} With the rapid development of high-speed rail systems, high-speed trains (HST) traverse mountainous terrain more frequently and

are susceptible to extreme wind conditions, which can decrease the operational safety of trains and even lead to accidents.^{5,6} In these accidents, passive anti-wind facilities such as wind barriers, windbreaks, and anti-wind open-cut tunnels have been applied to the railroad system, indicating the hidden risks of conventional anti-wind facilities. As shown in Fig. 1(b), there is a sudden change in the wind environment at the end or transition of anti-wind facilities (the region marked by the yellow dashed line) under crosswinds. When a train passes by this region, the rapid switching of the operating scenarios (protection and crosswind) will result in a violent transient aerodynamic impact on the



FIG. 1. Research background: (a) Twin mountainous terrain; (b) Passive anti-wind facilities.

train. In addition, these facilities are utilized to passively block crosswinds, but the contact area between the anti-wind facilities and the crosswinds potentially increases the aerodynamic forces exerted on facilities or bridges. Therefore, it is necessary to investigate new anti-wind measures to address the risk of HSTs overturning while traveling through twin mountains under crosswinds.

Under strong wind conditions, the aerodynamic performance of HST significantly deteriorates. This degradation is particularly noticeable when the trains encounter intense and rapidly changing airflow, leading to abrupt fluctuations in aerodynamic forces. Li *et al.*⁷ investigated the aerodynamic behaviors of HST under crosswind conditions by combining computational fluid dynamics (CFD) methods with a vehicle-track coupling model. The results revealed a decrease in operational safety of the HST under crosswinds. Xiao *et al.*⁸ analyzed the effects of the vehicle velocity, the crosswind velocity, and attack angle on the derailment mechanism and the dynamic response of the HST. They found that the operational stability of the HST is highly sensitive to crosswinds with an attack angle of 75° – 90° to the traveling direction, with the dynamic response and wheel-rail force of the train increasing linearly as wind speed rises. Transitioning from a calm to a crosswind environment results in a sudden and marked alteration in the aerodynamic behaviors of the HST. Deng *et al.*⁹ conducted a study on the transient effects of HST navigating through tunnel-bridge-tunnel terrains under crosswinds, indicating that trains encounter intense and momentary aerodynamic impacts after entering a crosswind environment. The behavior of HST operating on bridges is more directly affected by wind loads than the response of bridges.¹⁰ These studies demonstrate a significant positive correlation between crosswind speed and the operational safety of trains, wherein transient variations in crosswinds impose considerable instantaneous aerodynamic loads on HST. The acceleration effect of airflow and the uneven distribution of flow field characteristics are prevalent in mountainous regions. However, few researchers have focused on the aerodynamic characteristics of HST traversing through mountainous regions.

Mountainous regions are characterized by intricate and diverse geographical features, including high elevations, steep slopes, ridges, valleys, cliffs, and gorges. In strong wind conditions, these features tend to result in the acceleration effect. Yang *et al.*¹¹ observed wind field characteristics at a specific bridge-tunnel area in steep valley

terrain using ultrasonic anemometers, and further analyzed the spatial distribution of the wind field in the area using the large eddy simulation (LES) method. The acceleration effect at the tunnel entrance reached up to 37.5%, and the turbulence intensity and turbulence intensity ratio exhibited a lognormal distribution. Additionally, several studies have investigated wind field characteristics in specific gorge terrains using different field observation methods or numerical prediction methods.^{12–15} These methods and results are informative for wind field prediction and safety studies of buildings and transportation in mountainous areas. However, the complexity and variability of the terrain are significant features of mountainous areas in reality. Some scholars have summarized wind field laws for typical terrain in mountainous areas. For ideal V-shaped and U-shaped canyons, Zhou *et al.*¹⁶ used numerical simulation methods to analyze and summarize the influence of canyon parameters on the acceleration effect under crosswinds. They used canyon models obtained by simply stretching V-shaped and U-shaped sections without considering the shape characteristics of real mountains. Cheng *et al.*¹⁷ investigated boundary layer thicknesses and the influence of canyon widths on acceleration effects using the shear stress transfer (SST) k - ω turbulence model. The canyon model used in the research took into account the shape characteristics of typical canyons in reality. However, such long strips of canyons are not common in mountainous regions, and high-speed trains rarely pass through them. Liu *et al.*¹⁸ and Yang *et al.*¹⁹ simulated the atmosphere flows over typical three-dimensional hills based on the LES method, which can provide valuable information for studying typical mountain contour lines. However, their research objects were isolated hills where the acceleration effect exhibited little significance. The aforementioned studies have discussed the wind field in various terrains in mountainous areas but have overlooked the common twin mountainous terrains, especially the aerodynamic characteristics of HST passing through twin mountains.

In order to mitigate the impact of strong winds on HST traversing through mountainous regions, Zhang *et al.*²⁰ focused on reducing the aerodynamic drag, lift, and lateral force of the head carriage of the HST subjected to crosswinds. They constructed a Kriging surrogate model between the head shape variables and its optimization objectives, resulting in the identification of Pareto-optimal head shapes after considering the main factors contributing to the optimization

objectives. Additionally, wind barriers installed alongside the bridge-tunnel sections of high-speed railways were found to block and divert crosswinds, weakening the effect of sudden changes in aerodynamic coefficients by over 30%.²¹ The height and ventilation ratio of these barriers significantly affected lateral and torsional displacements of bridges and vehicles.^{22–24} Yang *et al.*²⁵ compared the transient aerodynamic performance of HST passing through two types of windproof facilities (windbreaks and windproof open-cut tunnels) under crosswinds. They observed significant fluctuations in the five aerodynamic loads (lateral force, lift force, rolling moment, yaw moment, and pitching moment) of the HST during the period of entering or exiting the windproof facilities. Similarly, Chen *et al.*²⁶ analyzed the effects of the sudden transition of windbreaks on HST under crosswinds in terms of flow field structures and dynamic response. They found that the unreasonable structural geometry and the insufficient height of the windshields led to a deterioration in the dynamic characteristics of the train. As a result, blowing slots installed on the train surface were proposed to mitigate the effects of crosswinds, ultimately reducing the aerodynamic load coefficients of trains by 18.5%–30.8%.²⁷ While the blowing measure offers a new concept for windproofing HST, it is important to note that the control system of the measure requires a high level of intelligent recognition and the reaction force on the train may cause a negative effect.

In recent years, the current industrial air curtain machines are widely used to isolate and control the dust, heat, and smoke in buildings, such as malls, chemical laboratories, office buildings, and industrial plants (Fig. 2).^{28–30} Yang *et al.*³¹ discussed the operating performance of an air curtain machine applied to a small building using a wind tunnel test. To ensure the isolation performance of air curtains, it is necessary to control the velocity, continuity, width, and angle of the jet flow. Therefore, air curtain machines will cause significant noise and economic problems if directly applied in this study, and it is necessary to optimize the design of the air curtain machine for the application characteristics in future studies to address these issues. In fact, a series of ejectors that can create planar streams should work well in this study, and as a result, the shortcomings of air curtain machines

in terms of the large occupancy area and the high construction cost are overcome. In this study, a HST operating at 300 km/h (83.33 m/s) will pass through the twin mountain terrain within 4 s, and the jets only require to operate during the period when the train passes by, which effectively avoids the problem of high-energy consumption. In the twin mountain terrain, where wind resources are abundant, small or medium wind power generators are available to supply the energy required for the ejector. Due to the small size and short operating time of the ejectors, the noise problem and the impact on nature generated by ejectors can be alleviated. In addition, automatic on-off flaps are installed at the inlet and outlet of ejectors, considering the possibility of animal intrusion into ejectors.

In this study, wind speed tests and flow visualization studies in the twin mountains are conducted using wind tunnels, cobra probes, and high-speed cameras. The obtained results, including wind speed and flow structure, are compared with those obtained by the improved delayed detached eddy simulation (IDDES) method. Additionally, an air-jet measure is proposed to mitigate the acceleration effect in the twin mountains terrain under crosswinds. To analyze and optimize the air-jet measures, a three-dimensional dynamic model of the air-twin mountains–train is established using a CRH380B type HST. Poly-hexcore meshes and the IDDES method are utilized to construct the computational model. This paper discusses the effects of jet streams on the flow field and the HST in the twin mountains in terms of the flow field (wind speed, flow separation, and turbulence characteristics) and the aerodynamic loading of the trains. The results will be beneficial for the study of the wind field in the twin mountains and will serve as a reference for the design of windproof measures for HSTs.

II. METHODOLOGY

A. Twin mountains model

The computational domains, as shown in Fig. 3, are symmetrically distributed in the X -direction, with geometric features that are symmetrically consistent. The computational models are established based on a scaling ratio of 1:10, where the length (L) of the HST is 7.653 m, the width (W) is 0.326 m, and the height (H) is 0.389 m, to



FIG. 2. Air curtain machines being used in various scenarios.

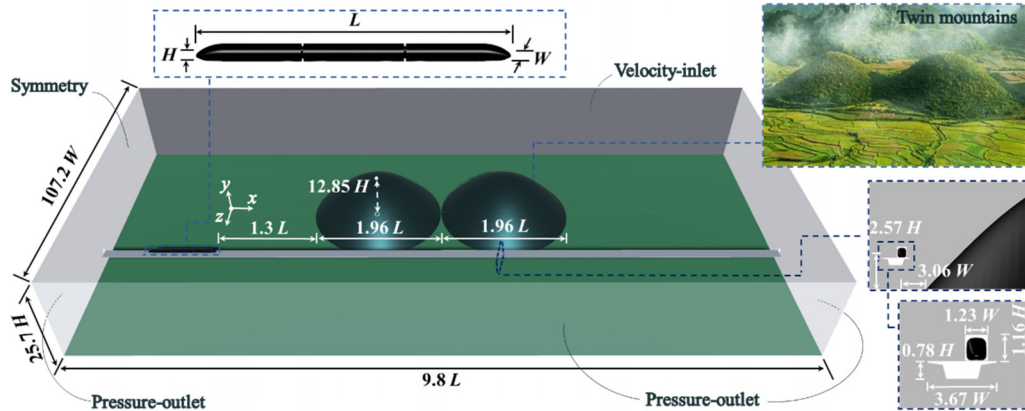


FIG. 3. Geometric characterization of the twin mountains computational model.

characterize the geometry of the computational model. The entire computational domain has a length of $9.8L$, a width of $107.2W$, and a height of $25.7H$. A cosine-type curve is used to construct the typical profile of the mountain, with the characteristics of this curve detailed in the article.³ The bottom diameter and the height of the mountains are $1.96L$ and $12.85H$, respectively, and the minimum spacing between the foothills of the twin mountains is 0 . In this study, three carriages (head, middle, and tail) of a CRH380B-type HST model are used to investigate the aerodynamic loads of the trains under crosswinds. The minimum distance of the initial position of the head carriage relative to the twin mountains is $1.3L$ in the X -direction. The gravity center of the HST is $2.57H$ from the ground in the Y -direction and $3.06W$ from the foot of the mountain in the Z -direction. The cross sections of the bridges adopt the typical box-type structure in Chinese high-speed railroad systems, with heights and widths of $0.78H$ and $3.67W$, respectively. The boundary at $15.3W$ upstream of the twin mountains is set as a velocity inlet to simulate the crosswinds with an airflow velocity of 30 m/s along the Z -direction ($U = 30\text{ m/s}$). In the computational model, the left, right, and downstream boundaries are defined as the pressure outlet, and a symmetric boundary is applied to the top surface. Other walls, such as the bottom of the model, the mountain

surface, the bridge deck, and the surface of the HST, are defined as the no-slip wall.

As shown in Fig. 4, the poly-hexcore grid is utilized to discretize the geometry into the grid model, with the grids at the front, back, and around the train defined as dynamic mesh. Three refined grid areas (C1, C2, and C3) are established around the twin mountains and the train to enhance the grid quality and result accuracy. Additionally, five layers of boundary grids are assigned to the surface of the twin mountains and the bridge, while 10 layers of boundary grids are assigned to the surface of the train, with an estimated $Y^+ \approx 2$. The final number of grid cells in the computational domain is 44×10^6 . The dynamic mesh technique is used to make the HST move along the X -direction at a velocity of 300 km/h ($\approx 83.33\text{ m/s}$). The general conservation equation for the dynamic meshes is shown in the following equation:

$$\frac{d}{dt} \int_V \rho \phi dV + \int_{\partial V} \rho \phi (\vec{u} - \vec{u}_d) d\vec{A} = \int_{\partial V} \mu \nabla \phi d\vec{A} + \int_V S_\phi dV, \quad (1)$$

where V , ρ , ϕ , and ∂V are the arbitrary control volume, the fluid density, the general scalar, and the boundary of the control volume, respectively; \vec{u} and \vec{u}_d are the velocity vectors of the flow and the

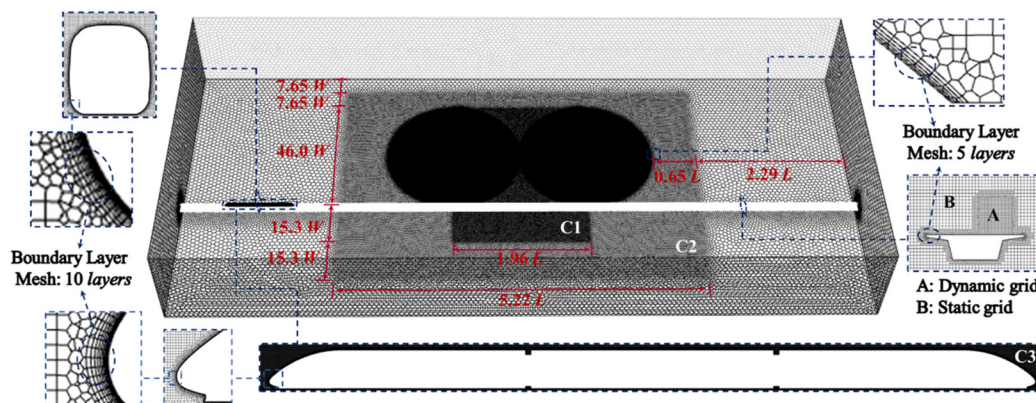


FIG. 4. Mesh characterization of the twin mountains computational model.

moving mesh, respectively; \vec{A} , μ , and S_ϕ represent the face area vector, the diffusion, and the source term of ϕ , respectively.

B. Solution strategy

Based on the calculated Reynolds number using the variables U_c , U_i , and H , it exceeds 2×10^6 , indicating that the flows in the twin mountains computational model belong to the high Reynolds number issue. The verification of the corresponding Reynolds number has been done in the work.³ In high Reynolds number scenarios, traditional Reynolds-averaged Navier–Stokes simulation (RANS) methods encounter challenges due to scale resolutions. High Reynolds number flows typically involve multi-scale turbulent structures, encompassing large-scale eddies and small-scale turbulence. The RANS method often struggles to accurately capture these turbulent structures at different scales simultaneously, leading to inaccuracies and distortions in the simulation results.^{32–34} The large eddy simulation (LES) method is particularly effective in capturing the large-scale structures of turbulence while modeling the smaller scales. However, the performance of LES is highly dependent on the quality of the subgrid-scale modeling and the fine grid resolution. The IDDES turbulence model provides a flexible and convenient scale-resolving method for high Reynolds number flows over complex terrain.³⁵ Therefore, the IDDES method based on the shear stress transport (SST) k – ω model is adopted in this research, and its governing equations are shown as follows:

$$\frac{\partial \rho k}{\partial t} + \nabla \cdot (\rho k \vec{U}) = \nabla \cdot \left[\left(\mu + \frac{\mu_t}{\sigma_{k3}} \right) \nabla k \right] + P_k - \rho \beta^* k \omega F_{IDDES}, \quad (2)$$

$$\begin{aligned} \frac{\partial \rho \omega}{\partial t} + \nabla \cdot (\rho \omega \vec{U}) = \nabla \cdot \left[\left(\mu + \frac{\mu_t}{\sigma_{\omega 3}} \right) \nabla \omega \right] + (1 - F_1) \\ \times \frac{2\rho \nabla k \cdot \nabla \omega}{\sigma_{\omega 2} \omega} + \alpha_3 \frac{\omega}{k} P_k - \rho \beta_3 \omega^2, \end{aligned} \quad (3)$$

$$F_{IDDES} = \frac{l_{RANS}}{l_{IDDES}}, \quad (4)$$

where k , ω , μ , and μ_t are the turbulence kinetic energy, the specific dissipation rate, viscosity, and the turbulent viscosity, respectively; F_1 denotes the SST blending function; P_k represents the production term of k ; and l_{RANS} and l_{IDDES} are the scale of length of the RANS and IDDES, respectively.

User-defined functions (UDF) are utilized to track and record the aerodynamic loads of the three carriages of the HST. Within the UDF, a time series of the aerodynamic loads of the carriages is obtained using an integration method based on the information of the pressures, the areas, and the coordinates of the mass centers of the face elements. The corresponding computational theory formulations are described in the article.³⁶ The computational time steps for the dynamic and static models are set to 5×10^{-5} and 1×10^{-4} , respectively, and the

corresponding Courant numbers are lower than 1. All computational work is conducted on the Wuxi supercomputer for a total of 14 days.

The aerodynamic loads are used to compare the aerodynamic performance of the HST under crosswinds with and without air jets. To facilitate the comparison and the analysis of the data, Eqs. (5)–(8) are used to express the dimensionless lateral force F_z , the rolling moment M_x , the yaw moment M_y , the pressure, and the time as follows:

$$F_i = \frac{1}{2} \rho S U_i^2 C_i, \quad (5)$$

$$M_i = \frac{1}{2} \rho S H U_i^2 C_{mi}, \quad (6)$$

$$C_p = \frac{2(p_j - p_0)}{\rho U_c^2}, \quad (7)$$

$$t = \frac{t' L}{U_i}, \quad (8)$$

where i denotes the direction of the three components of the load (takes x , y , and z); S is the side area of the carriage; C_i and C_{mi} are the coefficient of aerodynamic force and the aerodynamic moment coefficient, respectively; C_p , p_j , and p_0 represent the pressure coefficient, the pressure value, and the reference pressure in the environment, respectively; t is the time after the HST leaves from the initial position; and t' is the dimensionless time.

C. Air-jet scheme

Table I shows the geometrical characteristics and operating parameters of the FM-6020A air curtain. Table II describes the details of the cases established based on the IDDES method. The surfaces of the air curtain jet are parallel to the hillside, and the jet velocity of the air stream is defined as 25 m/s ($U_j = 25$ m/s). To explore the effect of the placement angle on the mitigation effect, the angles between the direction of arrangement of the air curtain machine and the X axis (jet angles) are divided into 0° , 15° , 30° , and 45° . The corresponding computational models with the arrangements of the air curtains are named cases II–V.

Figure 5 presents the installation locations of the air curtain on the twin mountains, and four colored lines represent the placement of the air curtains in the four air-jet scheme. The width of the jet (w) and the height (h) of the air curtain machine are determined to be 0.03 and 0.035 m, respectively, in the model with a scale ratio of 1:10. Designers rarely use viaducts in high-speed rail on hilltop locations for reasons related to safety and cost. Therefore, the air curtain machines are continuously installed on the slope of the hill, with the vertical height of the air curtain from the top of the mountain being $1.28H$. It has been estimated that a 90 kW motor power is required for the air curtain on one side of the hillside. Additionally, wind turbines are often installed in areas with high wind resources, and an ordinary wind turbine has a reserve power of 1500–2000 kW. To control the wastage of energy, the

TABLE I. Parameters of the air curtain.

Machine model	Rated frequency (HZ)	Rated voltage (V)	Motor power (W)	Air volume (m ³ /h)	Wind speed (m/s)	Size (m)
FM-6020A	50	380	2450	9400	25	$2 \times 0.3 \times 0.35$

TABLE II. Details of the cases.

Case	U_c (m/s)	U_j (m/s)	Jetting angle	U_t (m/s)
Case I	30
Case II	30	25	0°	...
Case III	30	25	15°	...
Case IV	30	25	30°	...
Case V	30	25	45°	...
Case VI	30	83.33
Case VII	30	25	0°	83.33
Case VIII	30	25	30°	83.33

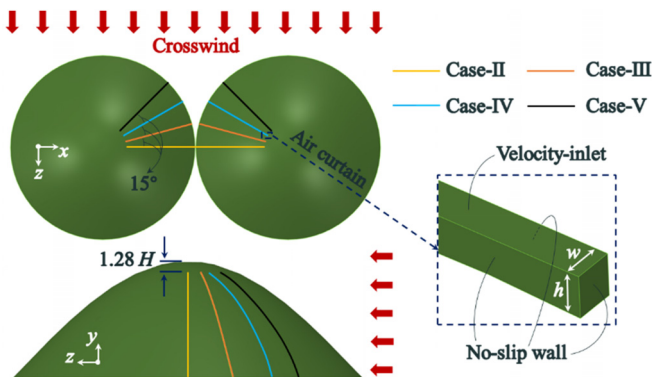


FIG. 5. Arrangement scheme of the air curtain.

operation of the air curtains is intelligently regulated by anemometers installed on the twin mountains and the management system of the high-speed railroad. Figure 6 presents the airflow formed by the air-jet device without the influence of crosswind at four instants (0.04, 0.08, 0.12, and 0.16 s) in case IV. The wind direction is set as vertical to the surface of the air curtain jet, and the air curtain machines formed a wind wall on the windward side of the twin mountains.

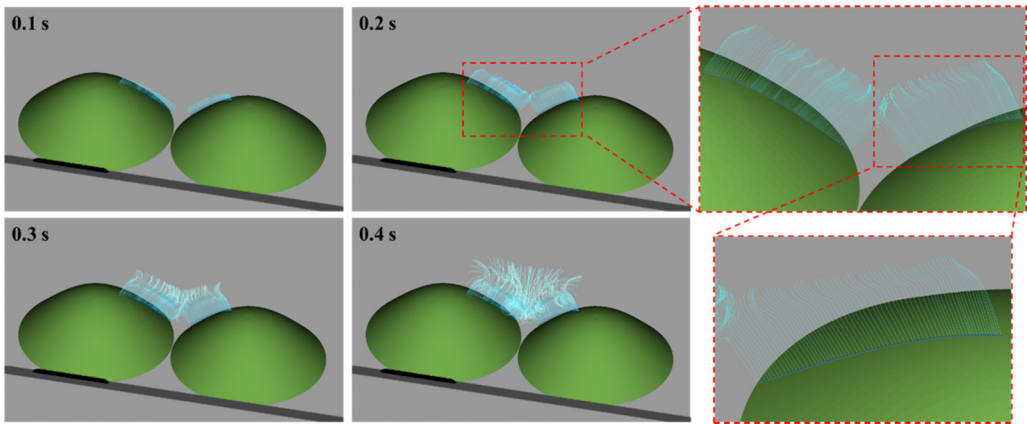


FIG. 6. Airflow formed by the air-jet device without the influence of a crosswind at four instants in the case IV.

D. Grid independence

As shown in Fig. 7, three grid resolutions (coarse, medium, and fine) of the twin mountains model are employed to verify grid independence, achieved by adjusting the cell sizes of the three refined grid regions (A1, A2, and A3). The corresponding number of grid cells for the three computational models are 34×10^6 , 44×10^6 , and 54×10^6 , respectively, calculated under the same environmental conditions ($U_c = 30$; $U_t = 83.33$; and $U_j = 0$ m/s).

Figure 8 compares the time course curves of the coefficient of the lateral force (C_z) and the rolling moment (C_{mx}) of the HST in three computational models (coarse, medium, and fine). The results demonstrate that the differences between medium and fine remain within 2.7%, and the differences between coarse and medium remain within 6.2%. Therefore, considering the accuracy of the results and the computational cost, the meshing strategy based on the medium is applied in this study.

III. WIND TUNNEL TEST

A. Wind speed

Figure 9 presents a test system based on the twin mountains model with a scaling ratio of 1:500, which is constructed in the WT2 wind tunnel at Central South University. The cross section of the test section in the wind tunnel has a height of 1.2 m and a width of 0.8 m, and the test system has a blockage ratio of 4.0%. In wind tunnel tests, a suitable blockage ratio is one of the key factors for obtaining reliable results in wind tunnel tests. Huang *et al.*³⁷ investigated the effect of blockage ratio on the aerodynamic behavior of rectangular prisms based on the wind tunnel test method. The effect of four blockage ratios (4.1%, 6.1%, 8.4%, and 10.1%) on the surface pressure coefficients and aerodynamic coefficients was analyzed by the synchronous pressure measurement technique. Yen *et al.*³⁸ analyzed the flow characteristics around a square cylinder in wind tunnel based on a blockage ratio of 4.0%. Therefore, a blockage rate of 4.0% and a scaling ratio of 1:500 are applied to the experiment. To ensure the accuracy of the data, the Cobra probe and an automobile measuring frame system are utilized for data acquisition. For further details on the experiments, corresponding CFD models, and discussions on the Reynolds number effects, refer to Ref. 3. Figure 10 compares the time course curves of

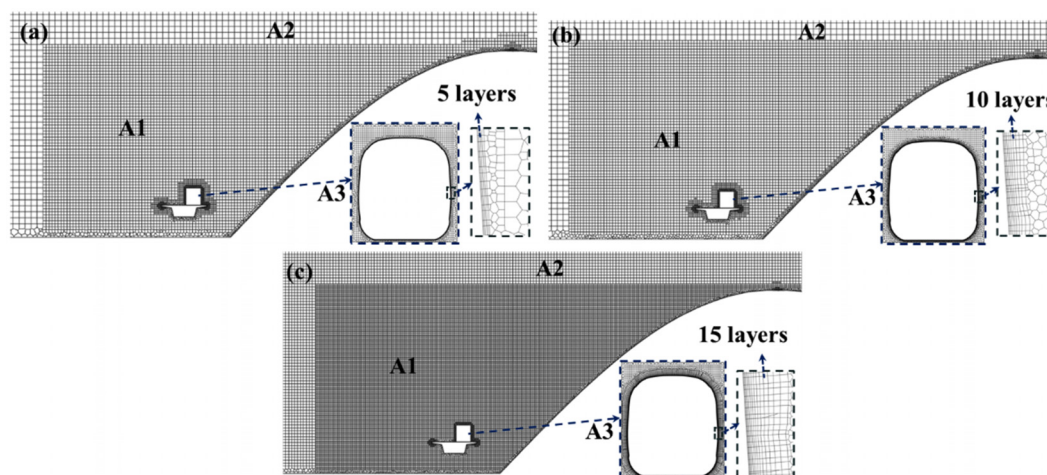


FIG. 7. Profiles of the twin mountains models with three grid resolutions: (a) coarse; (b) medium; and (c) fine.

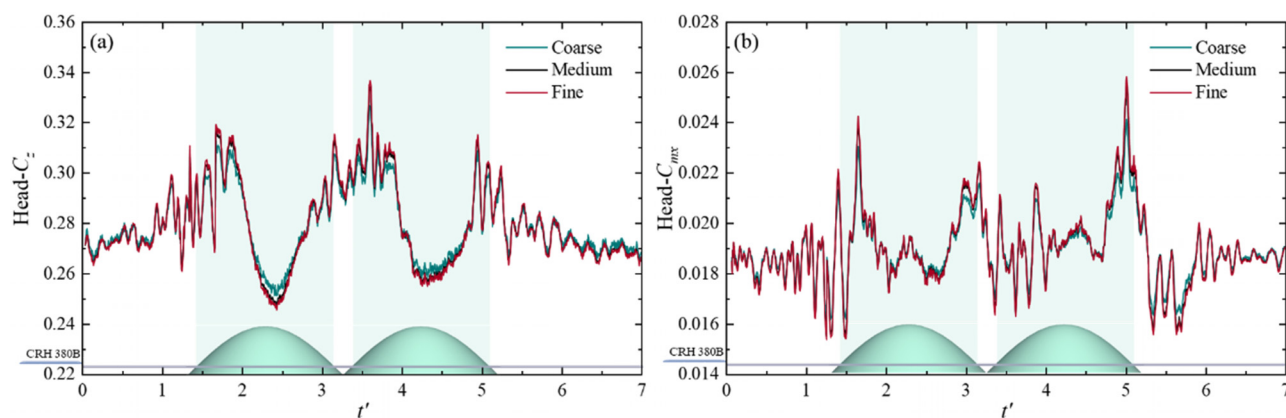


FIG. 8. Comparison of the time course curves of the coefficient of the aerodynamic loads on the HST in three computational models (coarse, medium, and fine): (a) lateral force and (b) rolling moment.

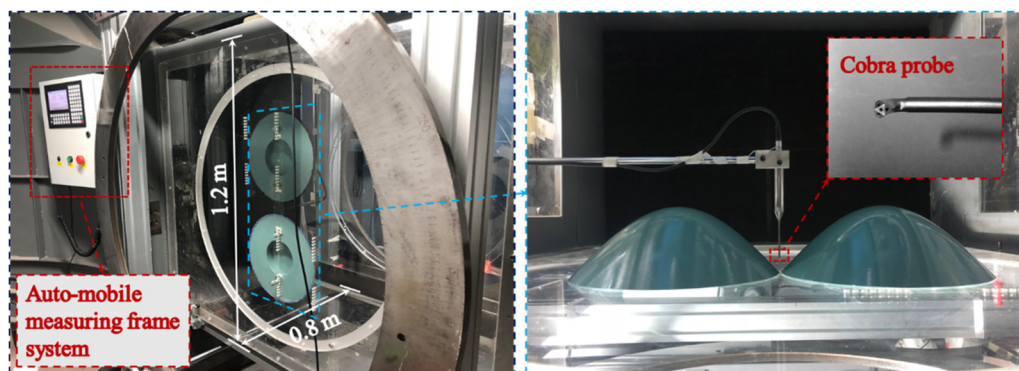


FIG. 9. Wind tunnel test system on the basis of the twin mountains model.

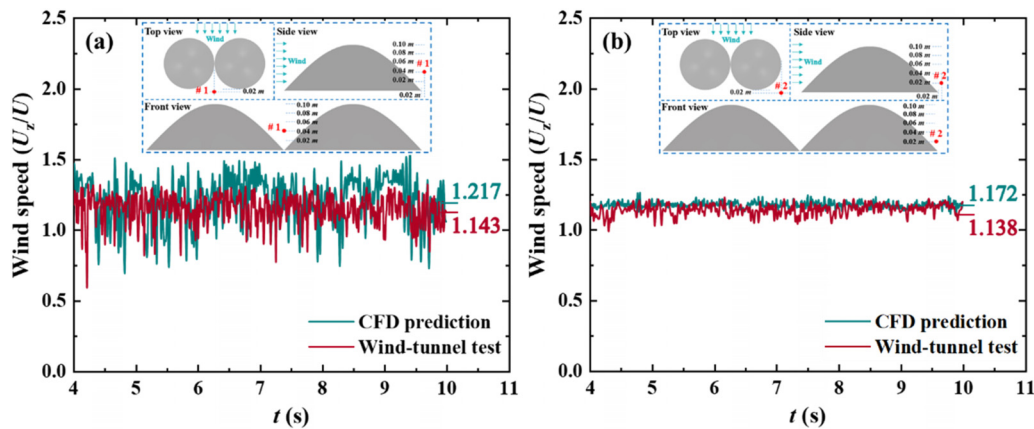


FIG. 10. Comparison of the time course curves of the Z component of the wind speed at typical points within 4–10 s: (a) #1 and (b) #2.

the Z component of the wind velocity at typical points (#1 and #2) within the 4–10 s duration in the wind tunnel tests and the IDDES method. In these instances, the Z-component of the wind velocity is normalized using the wind velocity of the incoming flow ($U = 29.6$ m/s). The fluctuations of the wind velocity at the points in the wind tunnel tests and the IDDES method are similar. The mean value of the Z component of the wind velocity at the point #1 (#2) in the IDDES method is 6.5% (3.0%) higher than those in the wind tunnel test. It can be considered that the results obtained based on the IDDES method in this paper are relatively consistent with the experimental results.

B. Flow visualization

Figure 11 presents the experimental system for the flow visualization of the flow field at the twin mountains. The corresponding IDDES model for flow visualization is established based on the experimental system (Fig. 12). In the experiment, white smoke is produced from the smoke wire generator under the control of the smoke wire instrument, and the smoke wires are formed by the smoke driven by the incoming flow. The smoke line generator is installed at heights of 0.02, 0.04, 0.06, and 0.08 m from the guide plate, which correspond to L_1 , L_2 , L_3 , and L_4 in Fig. 12. In order to prevent the smoke from being dispersed by

the high-speed incoming flow, the velocity of the incoming flow is set to 2 m/s. A high-speed camera with a capture frequency of 1000 Hz is used to record the development of the smoke wires flowing through the twin mountains, and the image quality of the smoke wires is optimized by adjusting the position and the illumination angle of the three light sources. Additionally, the guide plate is mainly used to simulate the ground and weaken the shear effect at the edge of the plate.

Figure 13 shows the flow evolution formed by the smoke wire generator at four different heights (0.02, 0.04, 0.06, and 0.08 m) in the flow field of the twin mountains during the wind tunnel test. The moment when the smoke wires move to the edge of the guide plate is considered the last moment (T_4), and the other three moments (T_1 , T_2 , and T_3) are determined at 0.02 s intervals. In the figure, dashed lines are used to mark the development of eddy structures in the downstream region of the center of the twin mountains. As shown in Fig. 13(a), numerous vortex structures are visible in the downstream region of the twin mountains at the height of 0.02 m. The incoming flow generates fine vortex structures due to the wind shear effect when passing through the twin mountains, and these vortex structures gradually evolve into larger scale vortex structures during development. Due to the dense distribution of the vortex structures, they interfere with each other, leading to frequent fluctuations in wind speed in this

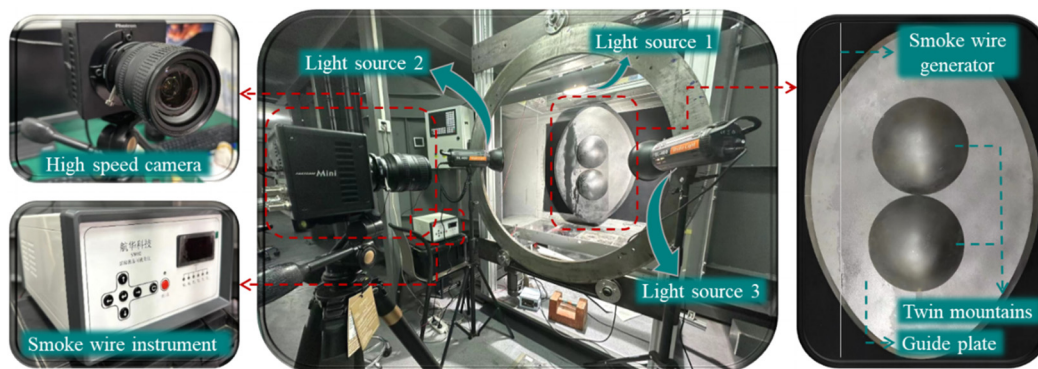


FIG. 11. Experimental system for the flow visualization of the flow field at the twin mountains.

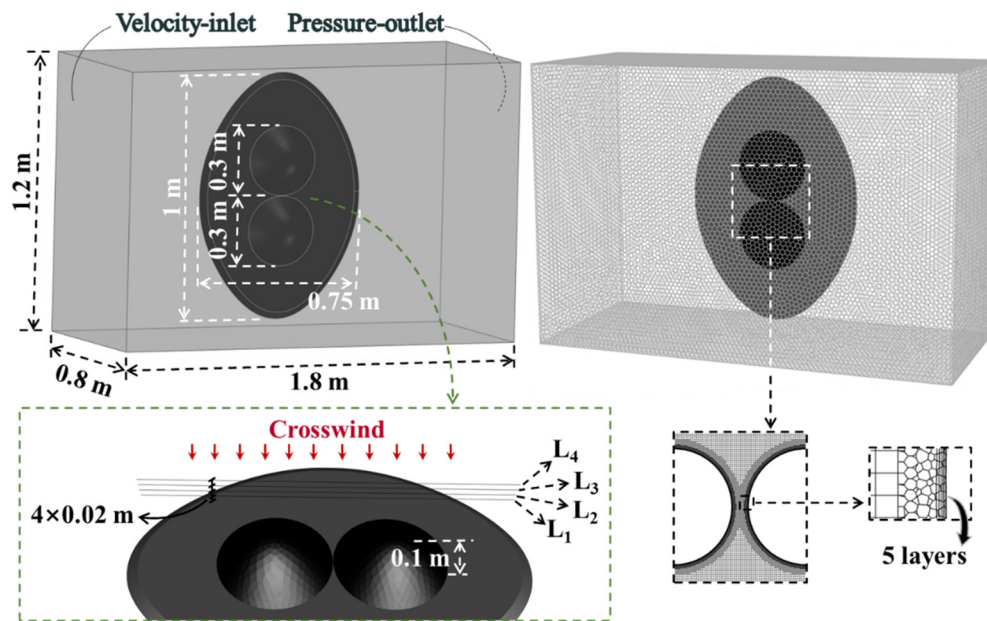


FIG. 12. CFD model for the flow visualization of the flow field at the twin mountains.

region. In Figs. 13(b)–13(d), the number of vortex structures in the downstream region of the center of the twin mountains gradually decreases as the height of the smoke wire generator increases. This is attributed to the gradual weakening of the acceleration effect with the increased height of the smoke wire generator. Particularly, at the height of 0.08 m, the smoke wires are uniformly distributed in the leeward region of the twin mountains.

Figure 14 compares the results of the flow visualization at the four heights of the twin mountains at the moment of T_4 based on the test and the IDDES method. The green and yellow dashed lines are used to mark the flow characteristics of the outer and inner regions of the twin mountains, respectively, under the same incoming flow conditions. As shown in Figs. 14(a)–14(c), the distribution characteristics and the development direction of the vortex structures of the flow field in the twin mountains based on the test and IDDES method are relatively consistent. The number of vortex structures decreases gradually as the height of the smoke wire generator increases, which is more evident in Fig. 14(d). In summary, the flow structures of the twin mountains obtained based on the IDDES method are close to the corresponding results of the tests.

IV. INFLUENCE OF THE JETTING ANGLE ON THE FLOW FIELD

A. Distribution of wind speed

Figure 15 compares the distribution of the Z component of the mean wind speed along the lines at four different heights ($2.57H$, $5.14H$, $7.71H$, and $10.28H$) in the different cases (cases I–V) during the 2–5 s interval. The positions of these four lines are denoted in the figure, and the mean wind speeds on the lines are normalized by the incoming wind speeds (U_c). Table III presents the details of the wind speed characteristics on the lines in the five cases depicted in Fig. 15.

Compared with the maximum values of the wind speed on the four lines in case I, the corresponding values in case II are reduced by up to 11.87%, while the corresponding values in cases III and V are only reduced by less than 4.5%. In case IV, the maximum values of the wind speed on the lines are reduced by up to 16%. In terms of the variation magnitude of the wind speed on the lines, the magnitude in case II is reduced by up to 30.4% compared to case I. Relative to the variation magnitude of the wind speed on the lines in case I, the reduction rates of the corresponding magnitudes in cases III and V are closer to each other, within 4.2%. The variation magnitude of the wind speeds on the lines in case IV is significantly lower than that in case I, and the reduction rate ranges from 25.6% to 80.9%. The mean wind speed distributions on the lines at the four heights in cases III and V are similar to those in case I, indicating that the air-jet devices in cases III and V did not significantly change the wind speed performances on the lines. The wind speeds on the lines in cases II and IV are generally lower than those in case I. Among them, in the middle of the line (near the $4.9L$ distance from the left outlet), the reduction of the wind speed in case II is greater than in case IV. This gap gradually narrows with the increase in the height of the line. Additionally, the wind speeds on the sides (near the $2.94L$ and $6.86L$ distance from the left outlet) of the line in case IV are lower relative to case II.

Based on the comparison of the peaks and variations in wind speeds on the lines, the critical areas and the wind field characteristics that may threaten the operational safety of the HST traveling along the lines can be identified. High wind speeds or substantial variations are primarily distributed in five regions on the lines (near the $2.94L$, $3.92L$, $4.9L$, $5.88L$, and $6.86L$ distance from the left outlet). The variation magnitude of the wind speed on the line at $2.57H$ above the ground is greater compared to those on the other three lines. Therefore, Fig. 16 shows the time course curves of the Z component of the wind speed at five typical measurement points located $2.57H$ above the ground in the five

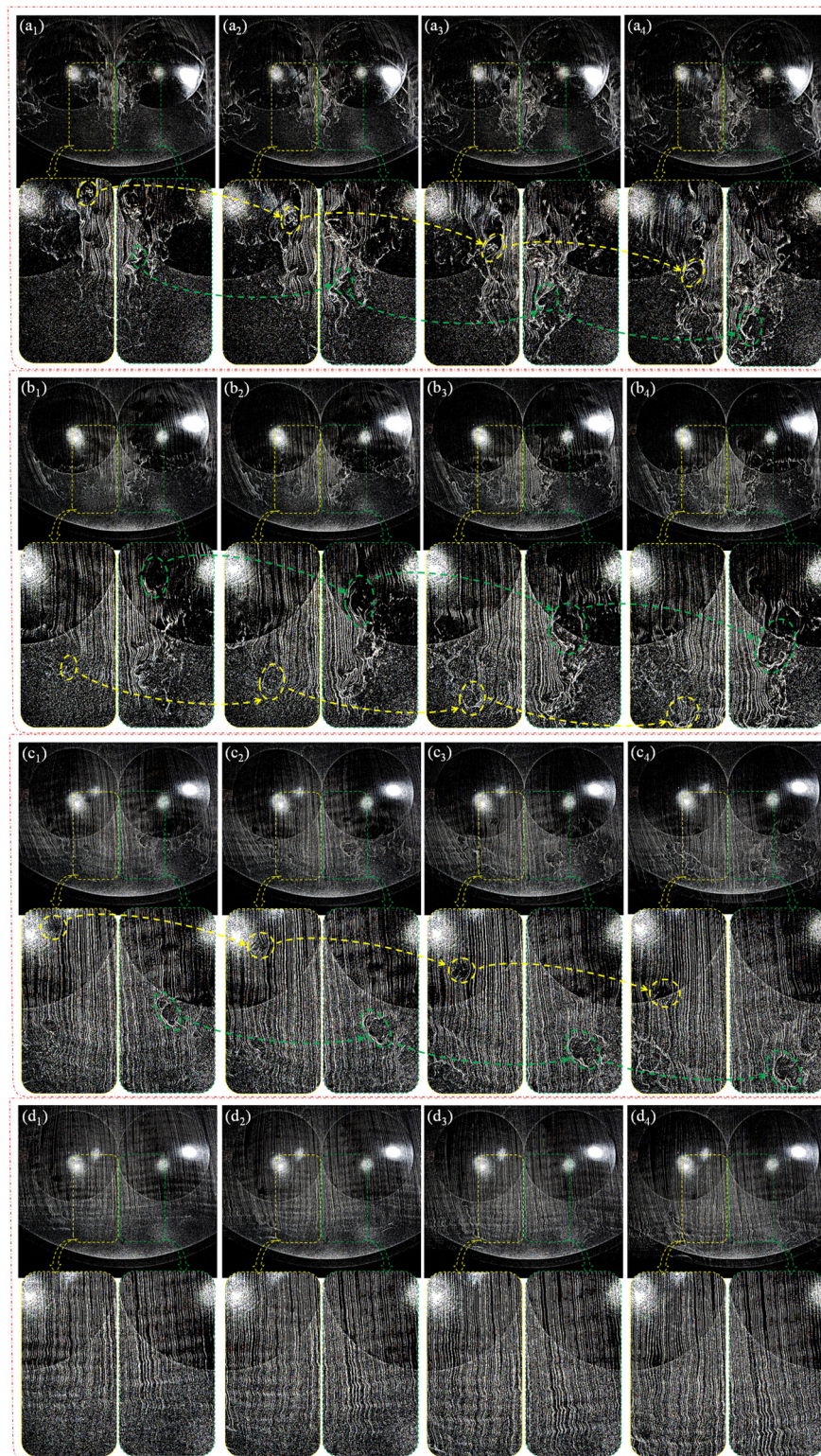


FIG. 13. Flow evolution formed by the smoke wire generator at the four heights of the flow field of the twin mountains in the wind tunnel test: (a) 0.02; (b) 0.04; (c) 0.06; (d) 0.08 m (subscripts 1, 2, 3, and 4 indicate the T_1 , T_2 , T_3 , and T_4 moments, respectively).

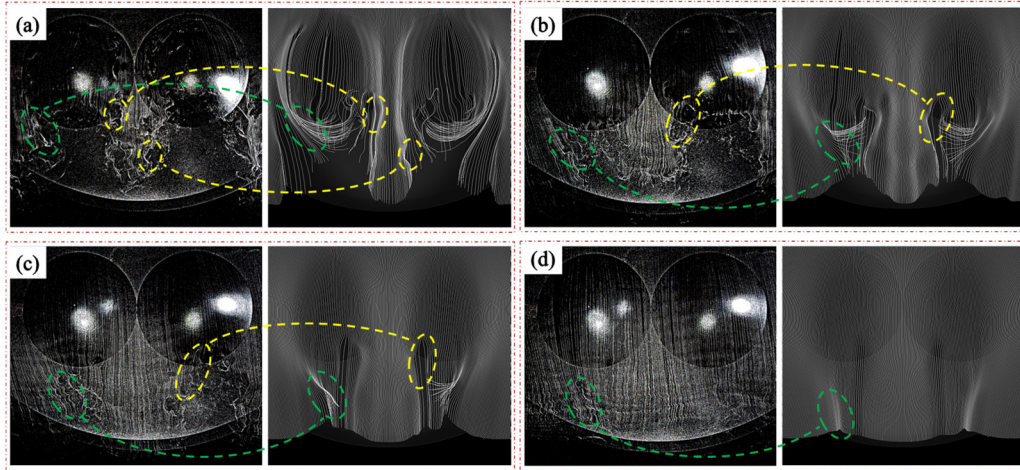


FIG. 14. Comparison of the results of the flow visualization at the four heights of the twin mountains at the moment of T_4 based on the test and the IDDES method: (a) L_1 ; (b) L_2 ; (c) L_3 ; and (d) L_4 .

cases during the 2–5 s timeframe. The details of the location of the five points are marked in the figure, and the wind speeds at the points are normalized using the incoming wind speeds (U_c). In addition, three moments are divided according to the characteristics of the time course curve of wind speed at the P3 point to facilitate the transient analysis of the flow field structure, marked with the yellow “ t_1 ,” “ t_2 ,”

and “ t_3 ” in the figure. Since the time course curves of the wind speeds at the P1 and P2 measurement points in the five cases are close to the performance of the wind speeds at P5 and P4, respectively, Table IV provides the mean, maximum, minimum, amplitude (Δ), and standard deviation (σ) of the wind speed at the three measurement points (P1, P2, and P3) in the five cases within the 2–5 s duration. In particular,

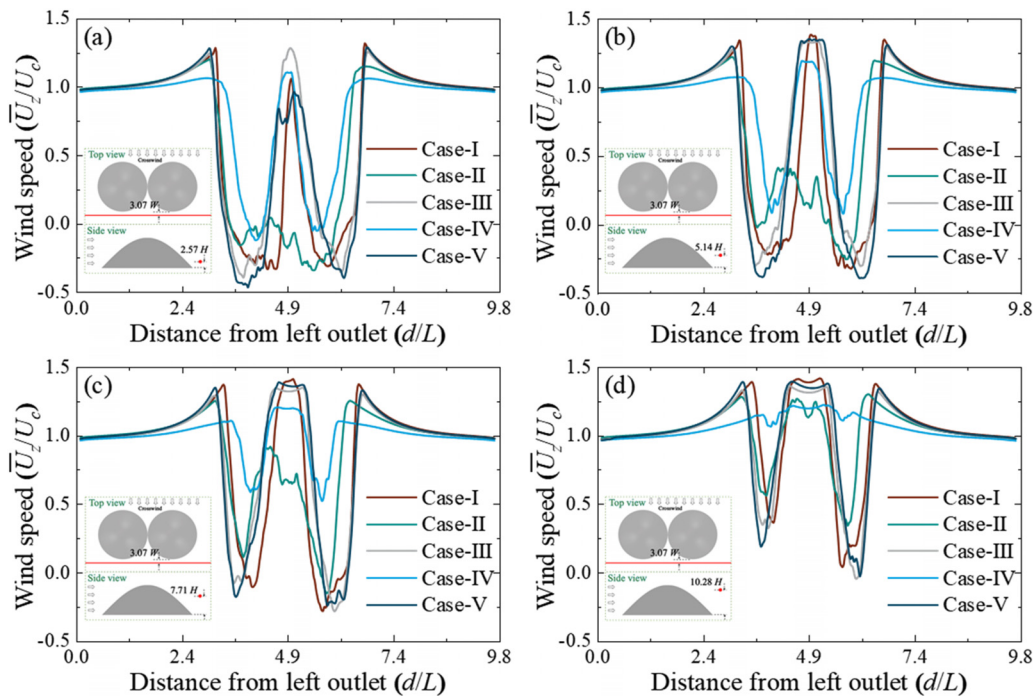


FIG. 15. Comparison of the distribution of the Z component of the mean wind speed along the lines at the four heights in the different cases during 2–5 s: (a) $2.57H$; (b) $5.14H$; (c) $7.71H$; and (d) $10.28H$.

TABLE III. Peaks and magnitudes of the Z component of the mean wind speed along the lines at the four heights in the five cases within 2–5 s.

Case	Height	$\bar{U}_{z\max}/U_c$	$\bar{U}_{z\min}/U_c$	Δ
Case I	2.57H	1.317	−0.333	1.65
	5.14H	1.382	−0.325	1.707
	7.71H	1.409	−0.285	1.694
	10.28H	1.415	0.036	1.379
Case II	2.57H	1.2	−0.342	1.542
	5.14H	1.218	−0.257	1.475
	7.71H	1.251	−0.154	1.405
	10.28H	1.299	0.339	0.96
Case III	2.57H	1.282	−0.395	1.677
	5.14H	1.33	−0.305	1.635
	7.71H	1.346	−0.286	1.632
	10.28H	1.36	−0.05	1.41
Case IV	2.57H	1.106	−0.122	1.228
	5.14H	1.189	0.075	1.114
	7.71H	1.204	0.519	0.685
	10.28H	1.222	0.959	0.263
Case V	2.57H	1.288	−0.467	1.755
	5.14H	1.348	−0.395	1.743
	7.71H	1.386	−0.245	1.631
	10.28H	1.39	−0.033	1.423

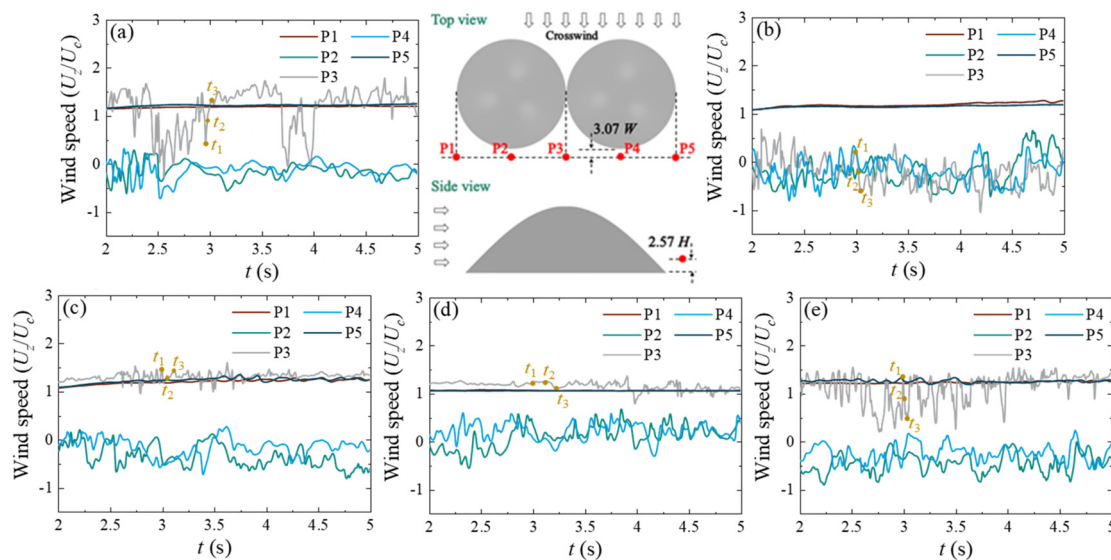
the table compares only the mean values of wind speeds at the P1 point in the five cases, as their wind speeds are stably distributed in the temporal domain.

As shown in Fig. 16 and Table IV, case I is taken as the basic case for analyzing the effect of the four jet angles on the wind speed at

TABLE IV. Mean, maximum, minimum, amplitude (Δ), and standard deviation (σ) of the wind speed at the three points in different cases within 2–5 s.

Measurement points	Case I	Case II	Case III	Case IV	Case V
P1 \bar{U}_z/U_c	1.193	1.193	1.212	1.068	1.239
P2 \bar{U}_z/U_c	−0.156	−0.198	−0.341	0.111	−0.453
$U_{z\max}/U_c$	0.294	0.658	0.209	0.683	0.002
$U_{z\min}/U_c$	−0.613	−0.717	−0.801	−0.547	−0.895
Δ	0.907	1.375	1.01	1.23	0.897
σ	4.89	9.054	6.968	7.293	5.935
P3 \bar{U}_z/U_c	1.176	−0.212	1.319	1.167	1.129
$U_{z\max}/U_c$	1.81	0.683	1.608	1.376	1.558
$U_{z\min}/U_c$	−0.273	−1.045	0.964	0.796	0.209
Δ	2.083	1.728	0.644	0.58	1.348
σ	12.706	8.577	2.206	2.426	8.877

typical measurement points. The mean wind speeds at point P1 in cases II, III, and V are similar to the corresponding values in case I, with differences of no more than 3.9%. However, the mean wind speed at point P1 in case IV is 10.5% lower than the corresponding value in case I. This indicates that the jet angle in case IV maximizes the reduction in wind speed at P1, consistent with the wind speed distribution on the sides (near the 2.94 and 6.86L distance from the left outlet) shown in Fig. 15. The mean wind speed at point P2 in cases II, III, and V increased by 0.042, 0.185, and 0.297, respectively, compared to case I, while the mean wind speed at point P2 in case IV is opposite to that in case I. This negative value indicates wind shear near P2 due to its location on the leeward side (LWS) of the twin mountains, and the change in the direction of the mean wind speed suggests that the jetting stream in case IV has minimized the wind shear near P2. The standard deviation of the wind speed at P2 in cases II–V increased by

**FIG. 16.** Comparison of the time course curves of the Z component of wind speed at the typical measurement points with the different jetting angles during 2–5 s: (a) case I; (b) case II; (c) case III; (d) case IV; and (e) case V.

85.2%, 42.5%, 49.1%, and 21.4%, respectively, compared to case I. As the jet angle decreases, the wind speed values at P2 become more varied in the temporal domain. The maximum wind speed at P3 in cases II–V decreases by 62.3%, 11.2%, 24.0%, and 13.9% compared to case I, respectively. The maximum wind speed fluctuations at P3 in cases II–V reduce by 17%, 69.1%, 72.2%, and 35.3% compared to the corresponding values in case I, respectively. It can be found that the jetting stream in case II significantly intercepts the incoming flow upstream of the P3, but does not significantly reduce the fluctuation of the wind speed. The jet streams in cases III and IV mainly restrain the performance of the wind shear in the wind direction.

B. Flow separation

Flow separation is a common phenomenon that occurs between the fluid and the boundary layer, often accompanied by the formation of vortex structures. Wall shear stress refers to the tangential stress between the fluid and the wall. When the wall shear stress is zero, it typically indicates that the fluid has separated or formed a stagnant zone at that particular location.³⁹ Figure 17 compares the distribution of mean Z-wall shear stress over the surface of the twin mountains in five different cases spanning 2–5 s. The color intervals for the wall shear stresses are set between -1 and 1 Pa in order to clearly distinguish regions where the wall shear stresses reach zero. The black region in the figure indicates locations where the mean Z-wall shear stress is zero, indicating flow separation at the surface of the twin mountains. The white line with arrows represents the number of flow separations

on the inner side of the twin mountains under varying jet conditions. The red dashed line marks the separation line on the outer side of the twin mountains, while the white dashed line represents four contour lines ($2.57H$, $5.14H$, $7.71H$, and $10.28H$) corresponding to the twin mountains.

In Fig. 17, a flow separation line is visible on the LWS of the twin mountains under crosswinds in case I. In case II, the two separation lines on the inside of the twin mountains result from the air curtain formed by the jet stream not closing at the foot of the mountain. However, the jet stream intercepted most of the incoming flow, leading to a significant reduction in wind speed and fluctuations at the P3 point [Fig. 16(b)]. In case III, two significant flow separations occur, and a tertiary separation appears in case IV under the combined action of the incoming flow and the jet stream. A tertiary separation also occurs in case V, but the range of the first and second separations is small, which has a limited effect on the wind speed at the P3 point, as evident in Figs. 16(a) and 16(e). On the outside of the twin mountains, the separation lines (red dashed lines) in cases III and V align more closely with those in case I, indicating that the jet streams in cases III and V have less influence on the flow field outside of the twin mountains compared to cases II and IV. In cases II and IV, the separation lines on the outer side of the twin mountains deviate inward relative to case I, and this deviation is particularly significant at all heights in case IV. As a result, the P2 (P4) point in the center of the LWS of the mountain is not affected by the separation flow, aligning with the phenomenon in Sec. III A, where the wind speeds near points P2 and P4

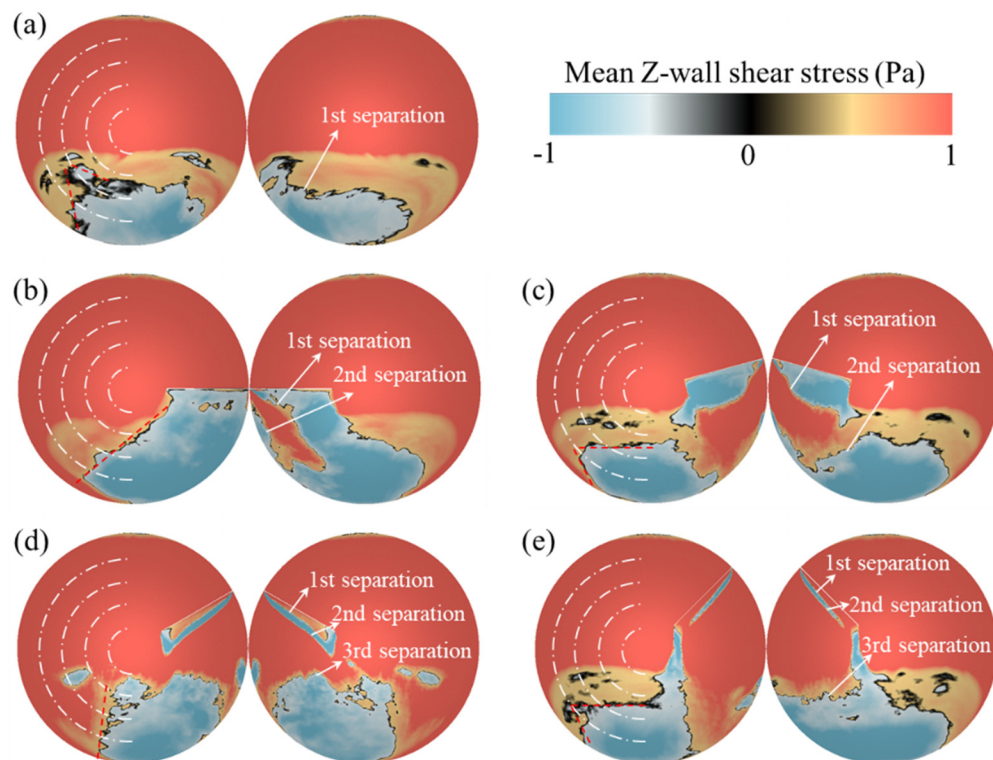


FIG. 17. Distribution of the mean Z-wall shear stress over the surface of the twin mountains in five cases during 2–5 s: (a) case I; (b) case II; (c) case III; (d) case IV; and (e) case V.

in case IV have increased compared to the corresponding values in case I, and the variation magnitude of the mean wind speeds on the measurement lines is reduced.

C. Turbulence intensity

Turbulence intensity reflects the relative intensity of pulsating wind speeds and provides critical insight into the characteristics of atmospheric turbulence motion. In Fig. 18, the distribution of mean turbulence intensity is compared across four horizontal sections ($2.57H$, $5.14H$, $7.71H$, and $10.28H$) in the five cases (cases I–V) during the 2–5 s time interval. A red dashed line in the figure delineates the region of high turbulence on the inner side of the twin mountains, while a blue dashed line marks the edge of the high turbulence region on the outside of the twin mountains. In case I, a large region of turbulence is observed on the inner zone of the twin mountains at a height of $2.57H$, attributable to the acceleration effect, gradually diminishing as the height increases. However, in case II, the jet stream alters the distribution of turbulence intensity of the twin mountains and accelerates the shedding of detached vortices. In cases III–V, the high turbulence regions at the four heights on the inner side of the twin mountains are reduced compared to case I, and the splitting of these high turbulence regions becomes more pronounced. This reduction weakens wind

speed fluctuations in the corresponding region and restrains the development of pulsating winds. Compared to case I, an expansion of the high turbulence region is observed on the outside of the twin mountains in cases III and V. Notably, there is a distinct low turbulence region on the outside of the twin mountains in case IV, and the edges of the turbulent region deviate inward relative to the other four cases. This is a result of tertiary separation and the third separation line deviating inward on the LWS of the twin mountains in case IV [Fig. 17(d)], wherein the incoming flow experiences frequent detachment and reattachment during bypassing motion on the surface of the twin mountains.

D. Transient evolution of the flow field

The transient evolutions of the flow field structure in the twin mountains are analyzed based on three moments selected from the time series of wind speeds at the P3 point in the five cases (cases I–V) shown in Fig. 16. Figure 19 illustrates the evolution of the wake vortex structure at three moments (t_1 , t_2 , and t_3) across the five cases. In this figure, vortex structures were identified based on the Q criterion ($Q = 8000$) and colored by the instantaneous magnitude of wind speed (U_m). A red dashed line is used to trace the growth process of a portion of the shed vortex structures from the incoming flow passing through

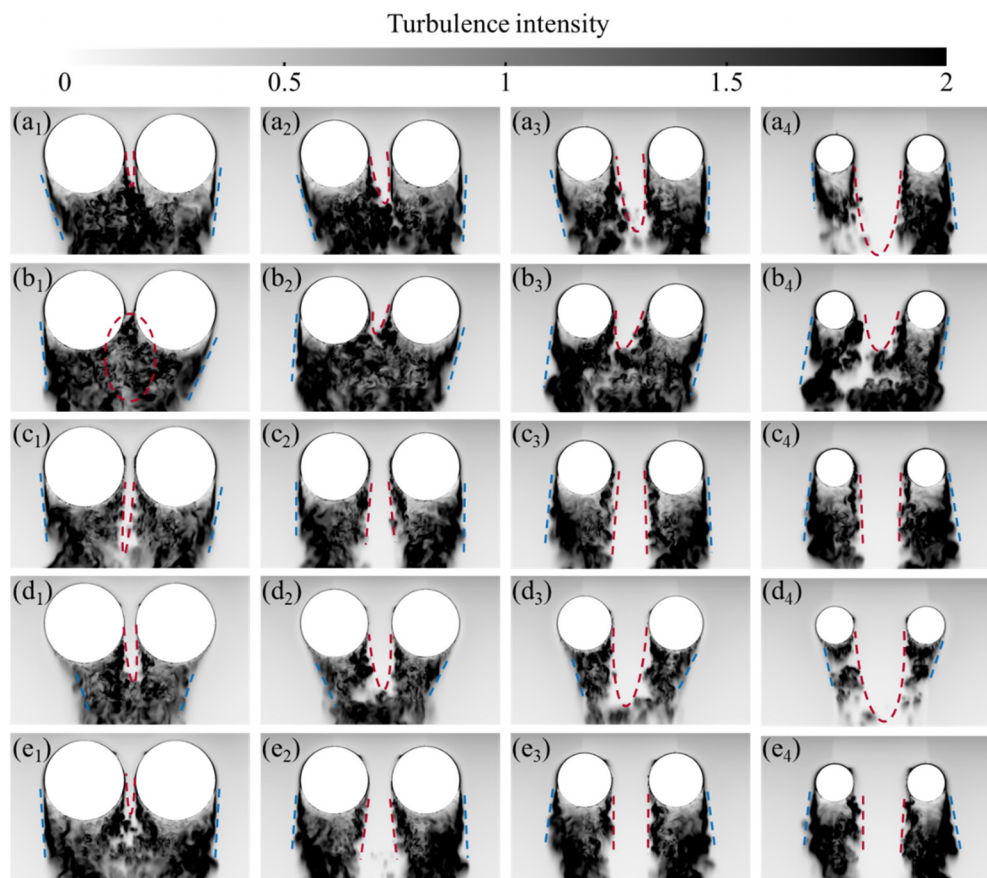


FIG. 18. Comparison of the distribution of the mean turbulence intensity in the four horizontal sections of the five cases during 2–5 s: (a) case I; (b) case II; (c) case III; (d) case IV; and (e) case V (subscripts 1, 2, 3, and 4 indicate that the horizontal profile is $2.57H$, $5.14H$, $7.71H$, and $10.28H$ from the ground, respectively).

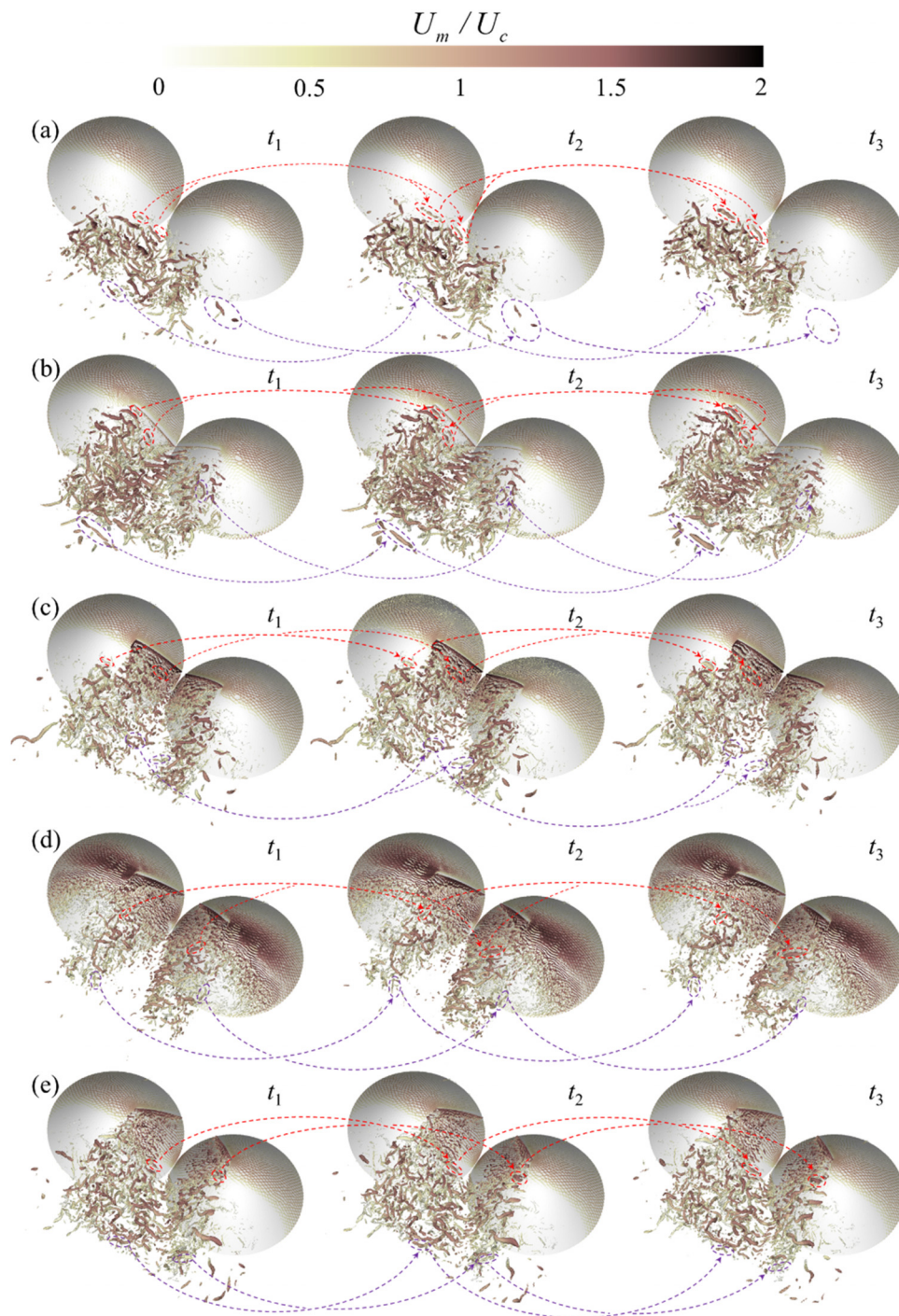


FIG. 19. Evolution of the wake vortex structure at three moments (t_1 , t_2 , and t_3) in the five cases: (a) case I; (b) case II; (c) case III; (d) case IV; and (e) case V.

the twin mountains, while a purple dashed line marks the dissipation process of a section of the large vortex structures.

In Fig. 19, there are numerous small vortex structures on the LWS of the twin mountains in case I when the incoming flow passes

through it. The vortex structures, as indicated by the red dashed lines, gradually evolve into large striped vortex structures in the temporal domain. Additionally, a multitude of disordered vortex structures, resulting from the interference of vortex structures with each other

due to the narrow passages in the twin mountains, can be observed downstream of the twin mountains. The large striped vortex structures moving toward the downstream and the sides are discernible based on the evolution of the vortex structures indicated by the purple dashed line, accompanied by splitting and volume reduction during their movement. In cases II–V, a significant number of detached vortices are observed on the LWS of the jet device, owing to the influence of the jet streams. This changes the shedding position of the vortex structure compared to case I. Notably, the number of detached vortices on the LWS of the jet device in case II is notably larger than that in case I, and its distribution characteristics are more complex. In cases III and IV, the detached vortices on the LWS of the twin mountains are distributed in a “V” shape (the slope line at the foot of the mountains). In case IV, a significant number of fine detached vortices are attached to the slopes of the twin mountains due to the deviation of the flow detachment line on the surface of the twin mountains [Fig. 17(d)]. Furthermore, the number of detached vortices and large vortex structures downstream of the twin mountains in case IV is notably less than that in case I. However, numerous irregularly distributed vortex structures are observed downstream of the twin mountains in case V, possibly due to incomplete air curtains formed by the jet stream, resulting in ineffective blocking of the incoming flow.

V. TWIN MOUNTAINS—HIGH-SPEED TRAIN DYNAMIC MODEL

A. Aerodynamic performance of the HST

The results in Sec. IV reveal that the jet streams in cases II and IV are the most effective in mitigating the acceleration effect. Compared

with the maximum values of the wind speed on the four lines in case I, the corresponding values in cases II and IV are reduced by up to 11.87% and 16%, respectively. Specifically, the jet stream in case II significantly decreases (by 62.3%) the maximum wind speed near the P3 point in the wind field compared to case I. In case IV, the variation magnitudes of the mean wind speed on the measurement lines are drastically reduced (25.6%–80.9%) compared to case I. Additionally, the jet stream in case IV mitigates the pulsating characteristics of the accelerating airflow and significantly decreases the high-intensity turbulence in the wind field. The distribution of mean wind speeds and turbulence intensity at the height of $2.57H$ from the ground is the most pronounced, and the most complex compared to the other three heights ($5.14H$, $7.71H$, and $10.28H$). Subsequently, bridge-train dynamic models are incorporated into cases I, II, and IV to analyze the effect of the jet stream on the aerodynamic load of the HST traversing the twin mountains, defined as cases V–VII, respectively. The trajectory of the mass center of the HST is considered to be the line $2.57H$ from the ground. When a HST passes through complex terrains, the fluctuation of aerodynamic loads on the head carriage is more pronounced compared to the middle and tail carriages in the studies.^{40–42} Therefore, the characteristics of the aerodynamic loads of the head carriage are used to analyze the mitigation effect of the jet stream on the acceleration effect in this study.

In Fig. 20, the time course curves of the aerodynamic loads on the head carriage of the HST passing through the twin mountains are compared under non-jet conditions (case V), 0° jet angle (case VI), and 30° jet angle (case VII). The extreme values, fluctuation amplitudes, and standard deviations of the aerodynamic loads on the head

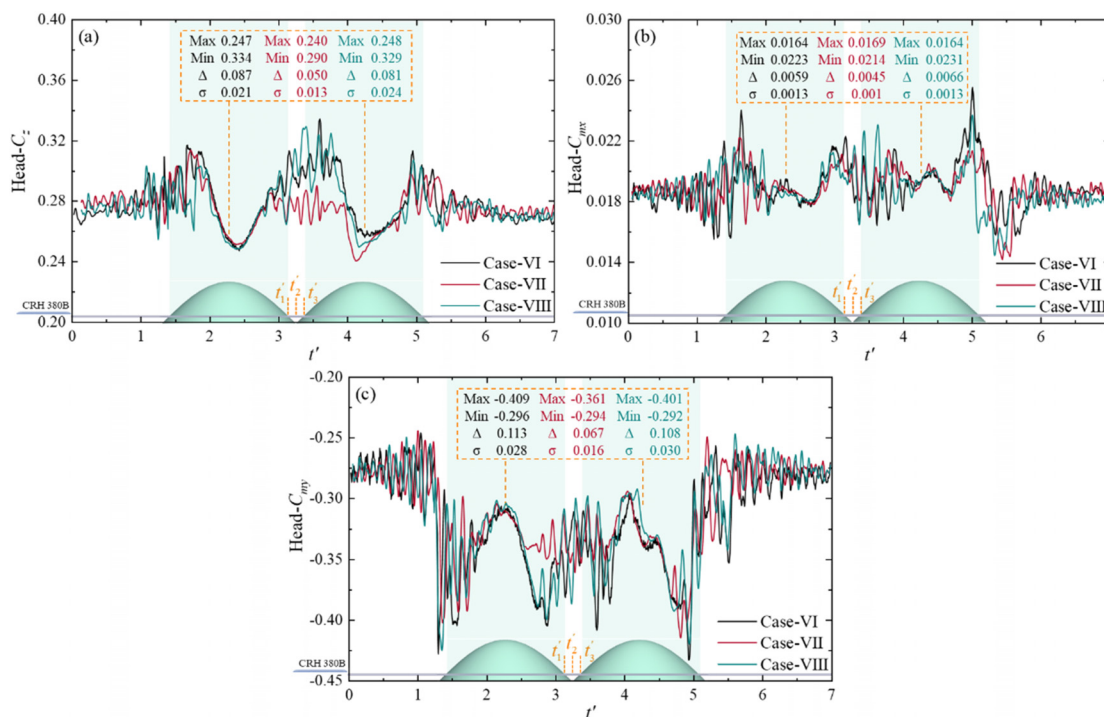


FIG. 20. Time course curves of the aerodynamic loads on the head carriage of the HST passing through the twin mountains: (a) lateral force coefficient; (b) rolling moment coefficient; and (c) yaw moment coefficient.

carriage of the HST traversing the inner side of the twin mountains are also shown. In case VI, the maximum values of lateral force, rolling moment, and yaw moment on the head carriage of the HST are reduced by 13.2%, 4.0%, and 11.6%, and the fluctuation amplitudes are reduced by 42.7%, 24.4%, and 40.7%, respectively, compared with case V. In case VII, the maximum values of lateral force and yaw moment on the head carriage of the HST are reduced by 1.5% and 2.1%, with the fluctuation amplitudes reduced by 7.3% and 4.8%, respectively, compared with case V. The mitigation effect of the jet stream with the 0° jet angle on the aerodynamic load of the HST subjected to the acceleration effect in the twin mountains is significantly better than that with the 30° jet angle.

B. Pressure characteristics

Figure 21 presents the evolutions of the distribution of surface pressure on the windward side (WWS) and the LWS of the head carriage in three cases (cases V–VII) at three moments (t_1' , t_2' , and t_3').

Each moment corresponds to the position reached by the nose of the head carriage (as illustrated in Fig. 20), and the pressure is dimensionless using Eq. (7). Positive and negative pressure zones are primarily located on the WWS and LWS of the head carriage, respectively. Contours with pressure coefficients of 1, 2, and 4 are marked on the WWS, while contours with pressure coefficients of -1 , -2 , and -4 are marked on the LWS. In Fig. 21(a), the area with a pressure coefficient higher than 4 is mainly distributed near the nose of the head carriage. The region surrounded by the contour with a pressure coefficient of 4 on the WWS gradually shifts toward the bottom with time, while the region enclosed by the contour with a pressure coefficient of 1 occupies most of the carriage surface under crosswinds. On the LWS, the region surrounded by the contour with a pressure coefficient of -4 moves toward the nose over time, and the region enclosed by the contour with a pressure coefficient of -1 develops toward the top and the tail of the carriage due to the frequent shedding of separating vortices at the top of the carriage under crosswinds. Comparing Figs. 21(a) and 21(b), it is observed that the high-pressure region on

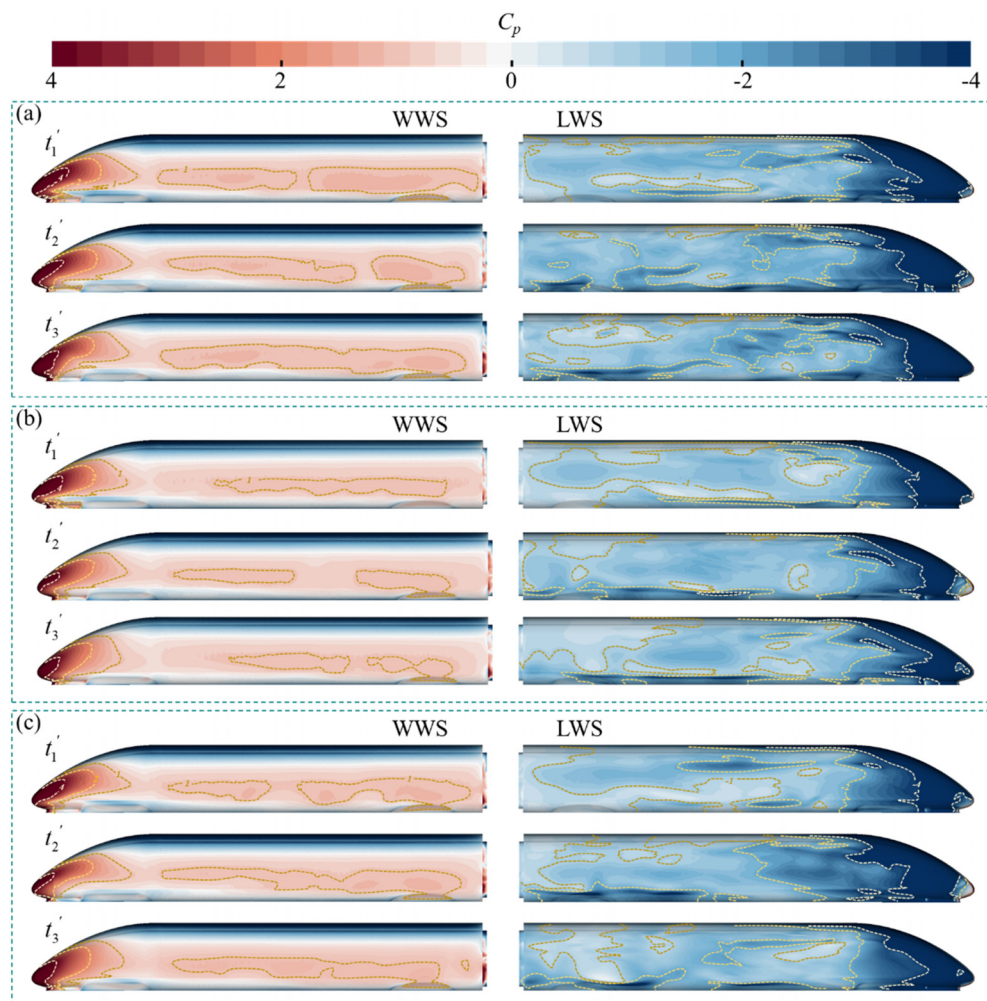


FIG. 21. Evolutions of the distribution of surface pressure on the WWS and the LWS of the head carriage at three moments (t_1' , t_2' , and t_3'): (a) case V; (b) case VI; and (c) case VII.

the WWS in case VI is significantly reduced compared to case V, while the low-pressure region on the LWS in case VI expands toward the bottom, indicating that the crosswind effect on the train passing the inner side of the twin mountains in case VI is attenuated by the jet stream. In comparison to Figs. 21(a) and 21(c), the region enclosed by the contour with a pressure coefficient of 4 in case VII has only slightly shrunk at moment t_2 compared to case V, with no significant difference in the region enclosed by the contour with a pressure coefficient of 1. Compared to Figs. 21(b) and 21(c), at moment t_2 , the area of the region enclosed by contours with a pressure coefficient of -2 and -4 on the LWS in case VII has significantly increased compared to case VI. Combined with the contents of Sec. IV, it can be concluded that the jet stream in case VII has not effectively reduced the wind speed performance on the measurement line at a height of $2.57H$ above the ground. Consequently, it has not exerted a better mitigation effect on the aerodynamic loads and pressures of the train than in case VI.

VI. CONCLUSIONS

After conducting a comparative study on the wind speed characteristics and flow structure of the twin mountains in a wind tunnel and CFD prediction, it was found that their differences in wind speed are maintained within 7%. The flow structures of the incoming flow during the bypassing process are relatively consistent, and the distinct acceleration effect is observed in the middle region of the twin mountains. To mitigate the acceleration effect, this study proposes an air-jet strategy based on the industrial air curtain. Based on the comparative study of different jet angles, the wind field characteristics of the twin mountains and the aerodynamic performances of the HST passing by the twin mountains are summarized as follows:

1. The wind velocity on the leeward side of the twin mountains increases up to 1.42 folds of the wind velocity of the incoming flow under crosswinds. Under the effect of jet streams with jet angles of 0° and 30° , the acceleration of the wind speed of the incoming flow bypassing the twin mountains is reduced by up to 11.87% and 16%, respectively.
2. There is an obvious flow separation on the mountain surface near the jet device, and the jet stream with a 0° jet angle shows the best closure effect compared to the other angles (15° , 30° , and 45°). In the case of the jet stream with a 30° jet angle, three significant flow separations are observed on the mountain surface.
3. Compared to the flow field of the twin mountains without the jet device, the case installed with a 0° jet angle shows larger areas of high turbulence and more vortex structures. However, the turbulence performance on the leeward side of the twin mountains is mitigated by the jet stream with a 30° jet angle. This is due to the greater wind shear effect of the incoming flow blocked by the jet stream with a 0° jet angle.
4. When the high-speed train passes downstream of the twin mountains area, the jet stream with a 0° jet angle proves more effective in reducing the aerodynamic loads on the train than the jet stream with a 30° jet angle. The 0° jet angle leads to a reduction of 13.2%, 4.0%, and 11.6% in the maximum values of the lateral force, the rolling moment, and the yawing moment of the train, and the fluctuation amplitudes are reduced by 42.7%, 24.4%, and 40.7%, respectively.

This work provides guidance for the theoretical study of wind field characteristics in mountainous areas. The air-jet strategy proposed to mitigate the acceleration effect in the twin mountains under crosswinds will provide a reference for windproof design, which is beneficial for the safe operation of the high-speed trains or the aircrafts passing through the area. The influence of the climatic environment (e.g., crosswind parameters, wind-rain, etc.) and the analysis of the dynamic response of the train will be considered in future work. Furthermore, feasibility is a key issue in the engineering field. The idea of jet mitigation measures in this study comes from the air curtain machines that are commonly applied in buildings. In the next work, it is necessary to consider the optimization of jet parameters, the design, and the application of jet devices in reality.

ACKNOWLEDGMENTS

This work was supported by the wind tunnel laboratory of the Central South University and funded by the National Natural Science Foundation of China (Grant No. 52308419), the Research Grants Council, University Grants Committee of the Hong Kong Special Administrative Region (SAR), China (Grant No. R-5020-18), the Innovation and Technology Commission of the Hong Kong SAR Government (Grant No. K-BBY1), the Science and Technology Research and Development Program Project of China railway (N2022G031), the Science and Technology Research and Development Program Project of China railway group limited (Major Project, 2022-Key-22), the Hong Kong Polytechnic University's Postdoc Matching Fund Scheme (Grant No. 1-W21Q), and the Science and Technology Research and Development Program Project of China railway group limited (Major Special Project, 2021-Special-01A).

AUTHOR DECLARATIONS

Conflict of Interest

The authors have no conflicts to disclose.

Author Contributions

Jian Wang: Investigation (lead); Software (lead); Writing—original draft (lead). **E. Deng:** Conceptualization (lead); Data curation (lead); Funding acquisition (equal); Methodology (lead); Project administration (lead); Supervision (lead); Writing—review & editing (lead). **Yi-Qing Ni:** Funding acquisition (equal); Resources (lead); Writing—review & editing (equal). **Xuhui He:** Resources (equal); Writing—review & editing (equal). **Pak Wai Chan:** Writing—review & editing (equal). **Wei-Chao Yang:** Funding acquisition (lead); Writing—review & editing (equal). **Huan Li:** Validation (lead). **Zu-Yu Xie:** Validation (equal).

DATA AVAILABILITY

The data that support the findings of this study are available from the corresponding author upon reasonable request.

REFERENCES

- ¹B. Blocken, T. van Hooff, L. Aanen, and B. Bronsema, "Computational analysis of the performance of a venturi-shaped roof for natural ventilation: Venturi-effect versus wind-blocking effect," *Comput. Fluids* **48**(1), 202–213 (2011).

- ²B. Li, Z. W. Luo, M. Sandberg, and J. Liu, "Revisiting the 'acceleration effect' in passage ventilation between two non-parallel buildings," *Build. Environ.* **94**, 714–722 (2015).
- ³J. Wang, X. Y. Liu, E. Deng, Y. Q. Ni, P. W. Chan, W. C. Yang, and Y. K. Tan, "Acceleration and Reynolds effects of crosswind flow fields in gorge terrains," *Phys. Fluids* **35**, 085143 (2023).
- ⁴M. A. Mohamed, D. Wood, and B. F. Ng, "Adding a simple production term to Reynolds-averaged Navier-Stokes turbulence models for flows over two-dimensional hills," *Phys. Fluids* **35**(6), 065135 (2023).
- ⁵R. G. Gawthorpe, "Wind effects on ground transportation," *J. Wind Eng. Ind. Aerodyn.* **52**, 73–92 (1994).
- ⁶W. C. Yang, E. Deng, M. F. Lei, P. P. Zhang, and R. S. Yin, "Flow structure and aerodynamic behavior evolution during train entering tunnel with entrance in crosswind," *J. Wind Eng. Ind. Aerodyn.* **175**, 229–243 (2018).
- ⁷T. Li, J. Y. Zhang, and W. H. Zhang, "A numerical approach to the interaction between airflow and a high-speed train subjected to crosswind," *J. Zhejiang Univ. Sci. A* **14**, 482–493 (2013).
- ⁸X. B. Xiao, L. Ling, J. Y. Xiong, L. Zhou, and X. S. Jin, "Study on the safety of operating high-speed railway vehicles subjected to crosswinds," *J. Zhejiang Univ. Sci. A* **15**, 694–710 (2014).
- ⁹E. Deng, W. C. Yang, L. Deng, Z. H. Zhu, X. H. He, and A. Wang, "Time-resolved aerodynamic loads on high-speed trains during running on a tunnel-bridge-tunnel infrastructure under crosswind," *Eng. Appl. Comput. Fluid Mech.* **14**(1), 202–221 (2020).
- ¹⁰P. A. Montenegro, R. Calçada, H. Carvalho, A. Bolkovoy, and I. Chebykin, "Stability of a train running over the Volga river high-speed railway bridge during crosswinds," *Struct. Infrastruct. Eng.* **16**(8), 1121–1137 (2019).
- ¹¹W. C. Yang, Y. K. Liu, E. Deng, Y. W. Wang, X. H. He, and M. F. Lei, "Characteristics of wind field at tunnel-bridge area in steep valley: Field measurement and LES study," *Measurement* **202**, 111806 (2022).
- ¹²H. M. Jing, H. L. Liao, C. M. Ma, Q. Y. Tao, and J. S. Jiang, "Field measurement study of wind characteristics at different measuring positions in a mountainous valley," *Exp. Therm. Fluid Sci.* **112**, 109991 (2020).
- ¹³Y. J. Sun and S. Zheng, "Large eddy simulation of atmospheric boundary flow over two two-dimensional hills," *Phys. Fluids* **35**(6), 061701 (2023).
- ¹⁴W. M. Ren, C. Pei, C. M. Ma, Z. G. Li, Q. Wang, and F. Chen, "Field measurement study of wind characteristics at different measuring positions along a bridge in a mountain valley," *J. Wind Eng. Ind. Aerodyn.* **216**, 104705 (2021).
- ¹⁵T. Zhou, Q. S. Yang, B. W. Yan, X. W. Deng, and Y. J. Yuan, "Detached eddy simulation of turbulent flow fields over steep hilly terrain," *J. Wind Eng. Ind. Aerodyn.* **221**, 104906 (2022).
- ¹⁶Z. L. Zhou, X. Xin, J. X. Yu, and M. Y. Liu, "Analysis of wind field characteristics of ideal V-shaped and U-shaped canyons," *Sustainability* **15**(13), 10011 (2023).
- ¹⁷J. H. Cheng, Z. X. Sun, S. J. Ju, G. W. Yang, J. Mao, and D. L. Guo, "Study on mathematical model construction of typical gorge wind field," *Eng. Appl. Comp. Fluid Mech.* **17**(1), 2249132 (2023).
- ¹⁸Z. Q. Liu, W. Wang, Y. Z. Wang, and T. Ishihara, "Large eddy simulations of slope effects on flow fields over isolated hills and ridges," *J. Wind Eng. Ind. Aerodyn.* **201**, 104178 (2020).
- ¹⁹Q. S. Yang, T. Zhou, B. W. Yan, M. Liu, P. V. Phuc, and Z. R. Shu, "LES study of topographical effects of simplified 3D hills with different slopes on ABL flows considering terrain exposure conditions," *J. Wind Eng. Ind. Aerodyn.* **210**, 104513 (2021).
- ²⁰L. Zhang, J. Y. Zhang, T. Li, and Y. D. Zhang, "A multiobjective aerodynamic optimization design of a high-speed train head under crosswinds," *Proc. Inst. Mech. Eng. Part F* **232**(3), 895–912 (2017).
- ²¹E. Deng, W. C. Yang, X. H. He, Z. H. Zhu, H. F. Wang, Y. W. Wang, A. Wang, and L. Zhou, "Aerodynamic response of high-speed trains under crosswind in a bridge-tunnel section with or without a wind barrier," *J. Wind Eng. Ind. Aerodyn.* **210**, 104502 (2021).
- ²²F. R. Xue, Y. Han, Y. F. Zou, X. H. He, and S. R. Chen, "Effects of wind-barrier parameters on dynamic responses of wind-road vehicle-bridge system," *J. Wind Eng. Ind. Aerodyn.* **206**, 104367 (2020).
- ²³H. Y. Xiang, H. Hu, J. Zhu, P. He, Y. L. Li, and B. Han, "Protective effect of railway bridge wind barriers on moving trains: An experimental study," *J. Wind Eng. Ind. Aerodyn.* **220**, 104879 (2022).
- ²⁴M. Mohebbi and A. M. Safaei, "The optimum model determination of porous barriers in high-speed tracks," *Proc. Inst. Mech. Eng., Part F* **236**(1), 15–25 (2022).
- ²⁵W. C. Yang, E. Deng, M. F. Lei, Z. H. Zhu, and P. P. Zhang, "Transient aerodynamic performance of high-speed trains when passing through two windproof facilities under crosswinds: A comparative study," *Eng. Struct.* **188**, 729–744 (2019).
- ²⁶Z. W. Chen, E. Z. Rui, T. H. Liu, Y. Q. Ni, X. S. Huo, Y. T. Xia, W. H. Li, Z. J. Guo, and L. Zhou, "Unsteady aerodynamic characteristics of a high-speed train induced by the sudden change of windbreak wall structure: A case study of the Xinjiang railway," *Appl. Sci.* **12**(14), 7217 (2022).
- ²⁷Z. W. Chen, Y. Q. Ni, Y. W. Wang, S. M. Wang, and T. H. Liu, "Mitigating crosswind effect on high-speed trains by active blowing method: A comparative study," *Eng. Appl. Comput. Fluid Mech.* **16**(1), 1064–1081 (2022).
- ²⁸C. Zhang, S. W. Yang, C. Shu, L. Z. Wang, and T. Stathopoulos, "Wind pressure coefficients for buildings with air curtains," *J. Wind Eng. Ind. Aerodyn.* **205**, 104265 (2020).
- ²⁹M. Juraeva, K. J. Ryu, S. H. Jeong, and D. J. Song, "Influences of the train-wind and air-curtain to reduce the particle concentration inside a subway tunnel," *Tunnelling Underground Space Technol.* **52**, 23–29 (2016).
- ³⁰J. W. Ji, W. Lu, F. Q. Li, and X. T. Cui, "Experimental and numerical simulation on smoke control effect and key parameters of Push-pull air curtain in tunnel fire," *Tunnelling Underground Space Technol.* **121**, 104323 (2022).
- ³¹S. W. Yang, H. Alrawashdeh, C. Zhang, D. H. Qi, L. Z. Wang, and T. Stathopoulos, "Wind effects on air curtain performance at building entrances," *Build. Environ.* **151**, 75–87 (2019).
- ³²W. C. Yang, H. Yue, E. Deng, X. H. He, Y. F. Zou, and Y. W. Wang, "Comparison of aerodynamic performance of high-speed train driving on tunnel-bridge section under fluctuating winds based on three turbulence models," *J. Wind Eng. Ind. Aerodyn.* **228**, 105081 (2022).
- ³³T. Y. Tong, G. Minelli, J. B. Wang, X. F. Liang, and S. Krajnovic, "Numerical investigation of a high-speed train underbody flows: Studying flow structures through large-eddy simulation and assessment of steady and unsteady Reynolds-averaged Navier-Stokes and improved delayed detached eddy simulation performance," *Phys. Fluids* **34**(1), 015126 (2022).
- ³⁴L. Qiao, Y. Li, Y. Zhang, J. K. Xu, and J. Q. Bai, "A hybrid prediction model for transitional separated flows over rough walls," *Phys. Fluids* **34**(9), 094103 (2022).
- ³⁵M. S. Gritskevich, A. V. Garbaruk, J. Schuetz, and F. R. Menter, "Development of DDES and IDDES formulations for the $k-\omega$ shear stress transport model," *Flow Turbul. Combust.* **88**(3), 431–449 (2012).
- ³⁶D. H. Ouyang, E. Deng, W. C. Yang, Y. Q. Ni, Z. W. Chen, Z. H. Zhu, and G. Y. Zhou, "Nonlinear aerodynamic loads and dynamic responses of high-speed trains passing each other in the tunnel-embankment section under crosswind," *Nonlinear Dyn.* **111**(13), 11989–12015 (2023).
- ³⁷J. Huang, M. Gu, and Y. Gao, "Blockage effects on aerodynamics of isolated tall buildings under uniform turbulent flows," *J. Wind Eng. Ind. Aerodyn.* **212**, 104607 (2021).
- ³⁸S. C. Yen and C. W. Yang, "Flow patterns and vortex shedding behavior behind a square cylinder," *J. Wind Eng. Ind. Aerodyn.* **99**(8), 868–878 (2011).
- ³⁹Y. Jiao and C. P. Wang, "Visualization of separation and reattachment in an incident shock-induced interaction," *Proc. Inst. Mech. Eng., Part G* **235**(12), 1706–1716 (2021).
- ⁴⁰W. M. Zhai, J. Z. Yang, Z. Li, and H. Y. Han, "Dynamics of high-speed train in crosswinds based on an air-train-track interaction model," *Wind Struct.* **20**(2), 143–168 (2015).
- ⁴¹E. Deng, W. C. Yang, M. F. Lei, Z. H. Zhu, and P. P. Zhang, "Aerodynamic loads and traffic safety of high-speed trains when passing through two windproof facilities under crosswind: A comparative study," *Eng. Struct.* **188**, 320–339 (2019).
- ⁴²D. Zhou, C. J. Xia, L. L. Wu, and S. Meng, "Effect of the wind speed on aerodynamic behaviours during the acceleration of a high-speed train under crosswinds," *J. Wind Eng. Ind. Aerodyn.* **232**, 105287 (2023).